

Searching for Inflow toward Massive Starless Clump Candidates Identified in the **Bolocam Galactic Plane Survey**

Jenny K. Calahan¹, Yancy L. Shirley, Brian E. Svoboda, Elizabeth A. Ivanov, Jonathan R. Schmid, Anna Pulley, Jennifer Lautenbach, Nicole Zawadzki, Christopher Bullivant, Claire W. Cook, Laurin Gray, Andrew Henrici, Massimo Pascale, Carter Bosse, Quadry Chance, Sarah Choi, Marina Dunn, Ramon Jaime-Frias, Ian Kearsley, Joseph Kelledy, Collin Lewin, Oasim Mahmood, Scott McKinley, Adriana M. Mitchell, and Daniel R. Robinson

Steward Observatory, University of Arizona, 933 North Cherry Avenue, Tucson, AZ 85721, USA; jcalahan@email.arizona.edu Received 2018 January 3; revised 2018 April 19; accepted 2018 April 19; published 2018 July 23

Abstract

Recent Galactic plane surveys of dust continuum emission at long wavelengths have identified a population of dense, massive clumps with no evidence for ongoing star formation. These massive starless clump candidates are excellent sites to search for the initial phases of massive star formation before the feedback from massive star formation affects the clump. In this study, we search for the spectroscopic signature of inflowing gas toward starless clumps, some of which are massive enough to form a massive star. We observed 101 starless clump candidates identified in the Bolocam Galactic Plane Survey (BGPS) in HCO⁺ J = 1-0 using the 12 m Arizona Radio Observatory telescope. We find a small blue excess of $E = (N_{\rm blue} - N_{\rm red})/N_{\rm total} = 0.03$ for the complete survey. We identified six clumps that are good candidates for inflow motion and used a radiative transfer model to calculate mass inflow rates that range from 500 to 2000 M_{\odot} Myr⁻¹. If the observed line profiles are indeed due to large-scale inflow motions, then these clumps will typically double their mass on a freefall time. Our survey finds that massive BGPS starless clump candidates with inflow signatures in HCO⁺ J = 1-0 are rare throughout our

Key words: ISM: clouds – ISM: molecules – ISM: structure – stars: formation

1. Introduction

Massive $(M > 8 M_{\odot})$ stars form from dense prestellar cores within massive molecular clumps (McKee & Ostriker 2007). The theories of the dominant physical mechanisms responsible for their formation are still polemical (Motte et al. 2017). Do massive protostars form from the monolithic collapse of a massive $(M > 30 M_{\odot})$ prestellar core, or do protostellar cores accrete surrounding material and grow rapidly through a competitive accretion with the surrounding environment? This long-standing problem in the field of star formation can be addressed by looking for signatures of large-scale accretion, determining how often it occurs, and the rate at which material is accreting. In this paper, we present a spectroscopic survey of the optically thick, intermediate-density gas tracer, $HCO^{+}1-0$, searching for the signature of large-scale inflow in massive clumps in the Milky Way for which no signature of star formation has been previously detected.

Recent blind surveys of the Galactic plane at far-infrared through submillimeter wavelengths (i.e., BGPS, ATLASGAL, HiGAL, JPS; Ginsburg et al. 2013; Urquhart et al. 2014; Eden et al. 2017; Elia et al. 2017) have identified a population of tens of thousands of massive clumps $(M > 200 M_{\odot})$ that do not appear to be forming stars. These objects were classified as starless clump candidates (SCCs) in the evolutionary analysis of clumps identified in the 1.1 mm Bolocam Galactic Plane Survey (Svoboda et al. 2016). The typical SCC has a median mass of $230 M_{\odot}$, a size of 1 pc, a gas kinetic temperature (measured from NH₃ observations) of 13 K, and a starless phase lifetime that scales inversely with the mass of the clump (Svoboda et al. 2016). The clumps are starless candidates because current Galactic plane surveys are limited to detecting

protostars with luminosities $L > \sim 30 L_{\odot}$ at a distance of a few kiloparsecs (Svoboda et al. 2016). Even if there is a population of undetected low-mass protostars already forming in them, SCCs represent environments that are in an early stage of star formation and have not been severely disrupted by feedback from intermediate- or high-mass protostars (Matzner 2017). SCCs are ideal locations to search for evidence of large-scale flows that may be important in the formation of massive protostars.

A spectroscopic signature of inflow is the presence of a blue asymmetric, self-absorbed line profile, meaning that the line peaks at smaller velocities with respect to the v_{LSR} of the object and the line shape are double peaked with a clear self-abroption dip. The general conditions for the formation of this line profile are that the tracer must be optically thick enough to create selfabsorption with increasing excitation temperature and a favorable velocity field along the line of sight (i.e., the flow has a component projected along the line of sight). The presence of a blue asymmetric self-absorbed profile is not evidence of inflow alone, as other physical mechanics (namely, rotation and outflow) can also mimic similar line shapes under the appropriate conditions (see Evans 2003). Generally, a convincing case can be made when the spectral line profile is mapped over a core and radiative transfer models are used with independent constraints on the source physical structure, for instance, a density profile derived from dust continuum observations, to successfully model the observed line profile. Convincing collapse signatures seen in emission have been observed toward individual dense cores (e.g., Choi et al. 1995; Myers et al. 1995; Narayanan et al. 1998; Tafalla et al. 1998; Evans et al. 2005; Seo et al. 2011). Recently there have been observations of purported large-scale flows toward high-mass (Peretto et al. 2013), intermediate-mass (Kirk et al. 2013), and

¹ Senior Honors Thesis submitted at the University of Arizona.

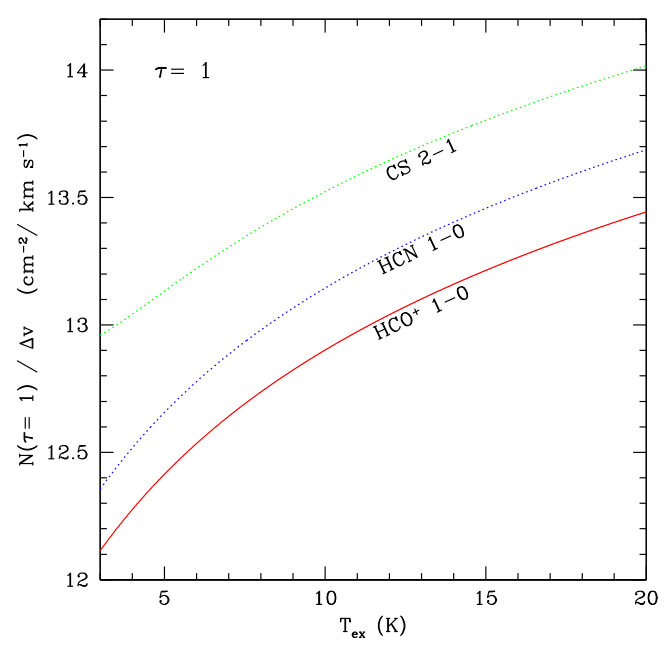


Figure 1. Column density at which a molecular tracer becomes optically thick (defined here as $\tau=1$) at the line peak plotted as a function of the excitation temperature. The curves were calculated assuming an FWHM line width of $\Delta \nu=1~{\rm km~s}^{-1}$. The HCN 1-0 curve has not accounted for hyperfine structure; the curve for the strongest HCN 1-0 hyperfine transition (F=2-1) would be the plotted curve multiplied by 9/5=1.8.

low-mass (Palmeirim et al. 2013) star-forming regions. A survey searching for the signature of inflow motions has not been performed yet toward the newly identified SCCs in the BGPS. A survey for inflow motions toward SCCs has the advantage that their kinematics should not be dominated by outflows since there is no detected star formation and therefore a blue asymmetric, self-absorbed profile is more likely to be associated with inflow.

For this survey, we chose the HCO $^+$ 1-0 line as an optically thick kinematic tracer of intermediate-density gas in SCCs. HCO $^+$ 1-0 has an effective excitation density of \sim 1000 cm $^{-3}$ (Shirley 2015). We can assess the column density at which a particular molecular tracer becomes optically thick using

$$\frac{N_{\tau=1}(T_{\rm ex})}{\Delta v} = 4\sqrt{\frac{\pi^3}{\ln 2}} \frac{\nu_{ul}^3}{g_u A_{ul} c^3} \frac{Q(T_{\rm ex})}{e^{-E_l/kT_{\rm ex}} - e^{-E_u/kT_{\rm ex}}},$$
 (1)

where $T_{\rm ex}$ is the excitation temperature of the rotational transition from $u \to l$ with energy levels E_u and E_l , frequency ν_{ul} , statistical weight g_u , and Einstein A_{ul} . $Q(T_{\rm ex})$ is the partition function assuming that every energy level has the same $T_{\rm ex}$ (the CTEX approximation; see Mangum & Shirley 2015). The threshold optically thick column density $N_{\tau=1}$ is a function of $T_{\rm ex}$ and the FWHM line width (Δv given in cm s⁻¹) where we have assumed a Gaussian line profile. Figure 1 shows these threshold column densities for commonly observed dense gas tracers assuming an FWHM line width of 1 km s⁻¹. Typical HCO⁺ column densities observed toward clumps in Galactic surveys are in the range of 10^{13} – 10^{15} cm⁻² (Hoq et al. 2013; Shirley et al. 2013), which is well above the threshold column density curve for all excitation temperatures $T_{\rm ex}$ < 12 K. HCO⁺ 1-0 is an excellent optically thick tracer of intermediate-density, subthermally populated gas with which to search for the

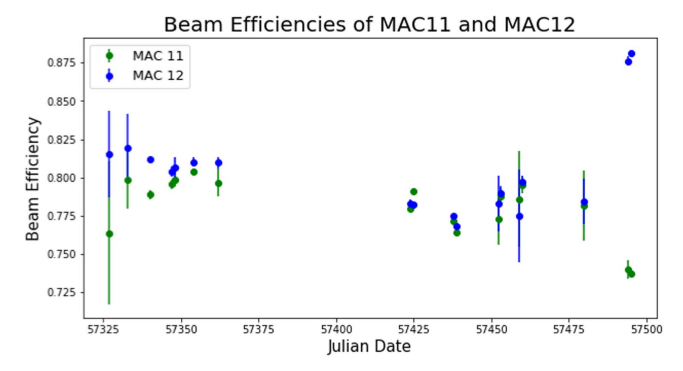


Figure 2. Main-beam efficiencies derived each day for each polarization (MAC 11 and MAC 12) and used for that day's data reduction. For MAC 11 the median value is 0.787, and for MAC 12 it is 0.801.

kinematic signatures of inflow. Simulations of global collapse agree with this assertion and further illustrate that the 1-0 transition is the best transition with which to search for inflow signatures (Smith et al. 2013).

In this paper, we present a systematic survey of 101 SCCs located toward the first quadrant of the Milky Way in HCO^+ 1-0 using the 12 m Arizona Radio Observatory telescope. We present the observations (Section 2) and analyze the line profiles searching the signature of inflow (Section 3). We find six inflow candidates and model their line profiles using the HILL5 radiative transfer model (Section 4). Finally, we calculate mass inflow rates and discuss how this may affect the evolution of these clumps (Section 4).

2. Observations

We observed at the Arizona Radio Observatory (ARO) 12 m radio telescope on Kitt Peak for 19 observing shifts between 2015 September and 2016 April.² We tuned to the J = 1-0transition of HCO⁺ at 89,188.5250 MHz in the lower sideband using the ALMA Band 3 ARO prototype dual-polarization sideband-separating receiver. Each polarization of the lower sideband was connected to the Millimeter AutoCorrelator (MAC) spectrometer (denoted MAC 11 and MAC 12) with $0.02 \,\mathrm{km \, s}^{-1}$ (6.1 kHz) resolution. The FWHM beam size at this frequency was 67. 6. Each source was observed for 60 minutes of total integration time where we position-switched between our source and an off position every 30 s. We identified clean off positions (no HCO⁺ J = 1-0 emission at the velocities of our sources) along the Galactic plane every half-degree. Observations of Jupiter and Venus were used to calibrate the spectra from the T_A^* scale to $T_{\rm mb}$ scale during each shift (Mangum 1993). Figure 2 shows the beam efficiencies for each polarization. The median $\eta_{\rm mb} = 0.787$ for MAC 11 and $\eta_{\rm mb} = 0.801$ for MAC 12. Our average baseline rms was $\sigma_{T_{\rm mb}} = 0.067 \, {\rm K}$ for the complete survey.

Sources were selected blindly from the starless clump candidate list in Svoboda et al. (2016) that had NH₃ (1,1) detections. The average distance of the sources was 4.3 kpc, with a range from 1.2 to 11.8 kpc. Our main-beam size on the 12 m is approximately 1.39 pc at that average distance. The average diameter of the sources is 2 pc, indicating that our single pointing observations cover most of the clump. Many of the sources had also been previously detected in HCO⁺ 3–2

 $^{^{\}overline{2}}$ This project was the group radio observing project of the undergraduate Astronomy Club at the University of Arizona.

Table 1Starless Clump Candidates

Source	α	δ	Distance	v _{LSR} (HCO ⁺) _{pk}	Our on	δν	
Source	(hh:mm:ss) ^a	(dd:mm:ss)	(kpc) ^b	(km s^{-1})	$(\operatorname{km} \operatorname{s}^{-1})$	OV.	$\sigma_{\delta u}$
BGPS 2427	18:9:33.88	-20:47:0.76	4.670	30.491	0.045	-0.108	0.032
BGPS 2430	18:8:49.41	-20:40:23.82	5.013	22.262	0.094	0.353	0.035
BGPS 2432	18:9:44.59	-20:47:10.21	4.369	29.002	0.036	-1.236	0.036
BGPS 2437	18:10:19.41	-20:50:27.45	4.437	-1.464	0.01	0.305	0.018
BGPS 2533	18:10:30.29	-20:14:44.2	4.975	30.623	0.121	-1.247	0.129
BGPS 2564	18:10:6.08	-18:46:5.64	3.013	29.404	0.038	-0.263	0.069
BGPS 2693	18:11:13.56	-17:44:54.85	2.103	18.695	0.115	-0.874	0.230
BGPS 2710 BGPS 2724	18:13:49.04	-17:59:33.25	1.200	34.246 34.428	0.027 0.115	-0.354 -0.543	0.029 0.045
BGPS 2724 BGPS 2732	18:14:13.61 18:14:26.85	-17:59:52.02 -17:58:50.93	1.185 1.191	34.428 35.082	0.113	-0.343 -1.189	0.043
BGPS 2742	18:14:29.1	-17:57:21.83	1.183	34.528	0.07	-0.542	0.038
BGPS 2762	18:11:39.52	-17:32:9.4	3.304	18.597	0.062	0.459	0.046
BGPS 2931	18:17:27.51	-17:6:8.42	3.285	23.119	0.04	0.564	0.067
BGPS 2940	18:17:17.15	-17:1:7.47	3.366	19.903	0.013	-0.061	0.009
BGPS 2945	18:17:27.35	-17:0:23.66	1.178	23.031	0.013	0.585	0.027
BGPS 2949	18:17:33.74	-16:59:34.94	1.279	22.352	0.025	-0.217	0.040
BGPS 2970	18:17:5.08	-16:43:28.66	3.568	40.159	0.02	0.102	0.016
BGPS 2971	18:16:48.12	-16:41:8.91	1.815	40.371	0.059	3.434	0.160
BGPS 2976	18:17:7.84	-16:41:14.59	1.830	40.413	0.022	0.902	0.032
BGPS 2984	18:18:18.23	-16:44:52.26	1.855	17.818	0.026	-1.170	0.062
BGPS 2986	18:18:29.68	-16:44:50.69	2.014	20.446	0.017	0.660	0.025
BGPS 3018	18:19:13.88	-16:35:16.47	6.522	19.27	0.045	0.281	0.043
BGPS 3030	18:19:19.68	-16:31:39.82	1.784	18.887	0.027	-0.180	0.046
BGPS 3110	18:20:16.27	-16:8:51.13	2.005	17.217	0.006	-0.219	0.008
BGPS 3114	18:20:31.5	-16:8:37.8	1.848	23.525	0.016	0.229	0.005
BGPS 3117 BGPS 3118	18:20:6.68 18:20:16.17	-16:4:45.75 -16:5:50.72	2.001 2.001	18.519 16.214	0.022 0.017	-0.032 -0.557	0.028 0.030
BGPS 3118 BGPS 3125	18:20:6.11	-16:3:30.72 -16:1:58.02	3.466	18.139	0.017	-0.557 -4.215	0.030
BGPS 3128	18:20:35.27	-16:4:53.81	4.170	19.044	0.040	-0.396	0.210
BGPS 3129	18:20:12.99	-16:0:24.13	4.289	18.812	0.046	-0.781	0.029
BGPS 3134	18:19:52.72	-15:56:1.56	4.083	20.658	0.004	0.139	0.010
BGPS 3139	18:20:34.24	-15:58:14	5.408	21.103	0.037	-0.805	0.057
BGPS 3151	18:20:23.19	-15:39:31.96	3.379	38.86	0.041	-0.614	0.048
BGPS 3220	18:24:57.03	-13:20:32.39	3.874	46.916	0.024	0.190	0.009
BGPS 3243	18:25:32.74	-13:1:31.05	4.597	68.069	0.019	-0.547	0.030
BGPS 3247	18:25:14.45	-12:54:16.74	4.447	44.886	0.2	-0.344	0.244
BGPS 3276	18:26:24.92	-12:49:30.07	3.379	66.515	0.047	-0.521	0.046
BGPS 3300	18:26:28.42	-12:37:3.98	11.668	62.427	0.031	-0.704	0.031
BGPS 3302	18:27:15.23	-12:42:56.45	11.785	64.66	0.044	-0.967	0.033
BGPS 3306	18:23:34.02	-12:13:52.79	4.777	57.082	0.016	-0.030	0.023
BGPS 3312	18:25:44.52	-12:28:34.11	5.271	47.098	0.012	-0.292	0.100
BGPS 3315	18:25:33.24	-12:26:50.63	4.793	47.678	0.021	2.111	0.184
BGPS 3344	18:26:40	-12:25:15.81	4.314	65.583	0.19	-0.132	0.227
BGPS 3442	18:28:13.51 18:28:27.26	-11:40:44.94	3.442 3.297	67.007 69.749	0.003 0.082	1.165 0.061	0.022
BGPS 3444 BGPS 3475	18:28:28.28	-11:41:33.99 -11:6:44.16	3.426	77.643	0.082	0.641	0.081 0.108
BGPS 3484	18:29:15.74	-11:0.44:10 -10:58:28.73	3.484	56.316	0.023	-0.017	0.108
BGPS 3487	18:29:22.77	-10:58:1.69	3.490	53.283	0.061	-0.459	0.071
BGPS 3534	18:30:33.45	-10:24:19	3.225				
BGPS 3604	18:30:43.92	-9:34:42.15	11.010	50.725	0.013	-0.770	0.017
BGPS 3606	18:29:41.95	-9:24:49.1	4.214	49.143	0.028	-0.419	0.054
BGPS 3608	18:31:54.82	-9:39:5.03	4.081	61.869	0.121	-0.597	0.041
BGPS 3627	18:31:42.32	-9:24:29.17	4.169	82.71	0.126	1.181	0.115
BGPS 3656	18:32:49.54	-9:21:29.26	3.906	77.655	0.061	0.215	0.042
BGPS 3686	18:34:14.58	-9:18:35.84	2.939	76.927	0.121	-0.301	0.103
BGPS 3705	18:34:32.69	-9:14:9.4	3.116	63.207	0.013	0.771	0.048
BGPS 3710	18:34:20.55	-9:10:1.94	2.505	74.405	0.024	-0.113	0.013
BGPS 3716	18:34:24.15	-9:8:3.6	3.146	75.039	0.082	-0.225	0.027
BGPS 3736	18:33:28.22	-8:55:4.36	5.031	65.62	0.016	0.139	0.018
BGPS 3822	18:33:32.06	-8:32:26.27	3.370	55.14	0.045	0.389	0.035
BGPS 3833	18:33:36.5	-8:30:50.7	4.493	56.113	0.044	0.403	0.036
BGPS 3892	18:35:59.74	-8:38:56.48	5.300	62.643	0.027	-0.816	0.015
BGPS 3922	18:33:40.98	-8:14:55.3	9.876	89.299	0.021	0.071	0.022

Table 1 (Continued)

(Continued)							
Source	α (hh:mm:ss) ^a	δ (dd:mm:ss)	Distance (kpc) ^b	$v_{\rm LSR}({\rm HCO^+})_{ m pk}$ $({\rm km~s^{-1}})$	$(\operatorname{km}^{\sigma_{\nu_{\mathrm{LSR}}}}_{\mathrm{s}})$	δν	$\sigma_{\delta v}$
BGPS 3924	18:34:51.17	-8:23:40.02	5.782	81.11	0.029	-0.089	0.017
BGPS 3982	18:34:30.79	-8:2:7.36	11.582	54.019	0.054	0.109	0.073
BGPS 4029	18:35:54.4	-7:59:44.6	3.539	80.687	0.027	-0.458	0.022
BGPS 4082	18:35:10.07	-7:39:43.55	5.084	98.994	0.027	-0.433	0.024
BGPS 4085	18:33:57.05	-7:29:31.43	5.087	96.409	0.025	-0.131	0.026
BGPS 4095	18:35:4	-7:36:6.46	5.353	114.384	0.06	1.359	0.061
BGPS 4119	18:36:29.65	-7:42:6.09	5.577	54.339	0.136	-0.352	0.050
BGPS 4135	18:37:44.06	-7:48:15.35	3.572	62.11	0.047	0.618	0.022
BGPS 4140	18:36:49.66	-7:40:36.83	3.617	96.106	0.025	0.114	0.032
BGPS 4145	18:36:52.95	-7:39:49.2	4.985	96.52	0.023	-0.010	0.022
BGPS 4191	18:37:4.58	-7:33:12.26	5.123	97.211	0.019	-0.226	0.016
BGPS 4230	18:35:50.85	-7:12:23.58	5.034	109.337	0.052	1.604	0.065
BGPS 4294	18:38:51.58	-6:55:36.52	5.688	58.936	0.146	2.106	0.115
BGPS 4297	18:38:56.37	-6:55:8.44	4.973	59.254	0.025	0.464	0.024
BGPS 4346	18:38:49.58	-6:31:27.06	5.823	95.56	0.111	0.741	0.030
BGPS 4347	18:38:42.93	-6:30:27.83	5.295	95.789	0.066	1.196	0.037
BGPS 4354	18:38:51.42	-6:29:15.38	5.840	93.949	0.085	-0.013	0.045
BGPS 4356	18:37:29.48	-6:18:12.13	4.453	110.176	0.021	0.143	0.014
BGPS 4375	18:39:10.19	-6:21:15.9	3.793	92.913	0.014	-0.160	0.019
BGPS 4396	18:38:34.74	-5:56:43.97	4.266	112.998	0.027	0.241	0.026
BGPS 4402	18:39:28.64	-5:57:58.57	4.285	100.149	0.124	0.679	0.091
BGPS 4422	18:38:47.88	-5:36:16.38	3.917	111.503	0.049	0.728	0.054
BGPS 4472	18:41:17.32	-5:9:56.83	3.216	47.937	0.084	1.138	0.093
BGPS 4732	18:44:23.4	-4:2:1.21	3.782	89.609	0.074	1.020	0.060
BGPS 4827	18:44:42.45	-3:44:21.63	4.928	89.611	0.04	3.011	0.082
BGPS 4841	18:42:15.65	-3:22:26.19	4.266	83.534	0.031	-0.288	0.022
BGPS 4902	18:46:11.36	-3:42:55.73	4.656	84.262	0.136	0.050	0.056
BGPS 4953	18:45:51.82	-3:26:24.16	5.502	90.192	0.054	-0.328	0.033
BGPS 4962	18:45:59.61	-3:25:14.53	6.092	88.765	0.078	0.493	0.091
BGPS 4967	18:43:27.8	-3:5:14.94	3.681	81.2	0.021	0.697	0.025
BGPS 5021	18:44:37.07	-2:55:4.4	5.181	78.77	0.072	-0.843	0.049
BGPS 5064	18:45:48.44	-2:44:31.65	5.210	100.608	0.009	-0.081	0.011
BGPS 5089	18:48:49.88	-2:59:47.86	6.534	85.137	0.012	-0.042	0.015
BGPS 5090	18:46:35.81	-2:42:30.19	5.181	95.464	0.04	-0.554	0.036
BGPS 5114	18:50:23.54	-3:1:31.58	3.681	67.254	0.02	0.802	0.015
BGPS 5166	18:47:54.26	-2:26:7.11	6.092	102.403	0.019	-0.263	0.024
BGPS 5183	18:47:0.29	-2:16:38.63	6.534				
BGPS 5243	18:47:54.7	-2:11:10.72	5.210	96.62	0.048	0.708	0.048

Notes

(Shirley et al. 2013), but since that survey sacrificed spectral resolution (only 1.1 km s^{-1} channel width) for wide bandwidth, we are unable to use the existing 3-2 observations to systematically search for inflow in the SCC sample. Throughout this paper, we use the BGPS v2.0.1 catalog number (Ginsburg et al. 2013) for the source name (i.e., BGPS 4029). The observed sample is 101 objects in the first quadrant of the Galactic plane, with a median distance of 4.1 kpc (see Table 1). Figure 3 shows the comparison of the mass and peak mass surface density between the 12 m sample and the complete sample of SCCs with well-constrained distances (see Ellsworth-Bowers et al. 2015, for an explanation of how distances are determined toward BGPS clumps). The 12 m sample has a median mass of $300 M_{\odot}$ and is representative of the full range of observed mass, spanning masses up to $5550 M_{\odot}$ (BGPS 3114); however, the observed 12 m sample is biased to higher peak mass surface densities by a factor of ~2 compared to the

complete SCC sample with well-constrained distances (see Syoboda et al. 2016).

For the best inflow candidates (Section 3), we also made observations in $\rm H^{13}CO^{+}$ 1–0 at 86,754.2884 MHz. The optically thinner $\rm H^{13}CO^{+}$ observations were directly compared to the $\rm v_{LSR}$ from NH₃ observations (Svoboda et al. 2016) as a secondary check that an optically thin line peaks in the HCO⁺ 1–0 absorption dip. The spectrometer setup and subsequent analysis are identical to that of HCO⁺ 1–0 observations.

3. Results

3.1. Line Asymmetry Statistics

We observed a total of 101 starless clump candidates in HCO^+ J=1-0. Two of the spectra were not used for the subsequent analysis because they were nondetections at the NH₃ velocity (BGPS 3534 and BGPS 5183). All spectra were

^a All coordinates are epoch J2000.0.

b Distances are the maximum likelihood distance of the distance probability density function (DPDF) in Svoboda et al. (2016).

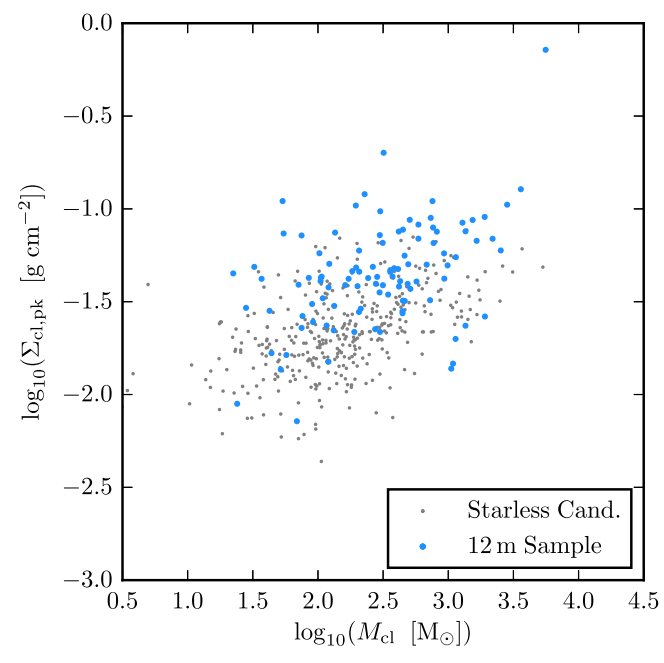


Figure 3. Mass and peak mass surface density of BGPS starless clump candidates with well-constrained distances. Each point corresponds to the median value of the mass and peak mass surface density probability density functions (see Svoboda et al. 2016). "12 m Sample" is the subset of sources observed in this paper.

visually analyzed to search for blue asymmetric line profiles with self-absorption dips (Figures 4 and 5). If NH₃ peaked in the self-absorption dip of a blue asymmetric profile, it was considered a candidate for inflow. We found that six of the 101 sources (6%) were good infall candidates. Their line profiles are shown in Figure 6. There are some negative velocities, which would suggest emission in the off positions, but any negative peaks are located far from the source spectra and will not affect the analysis.

We checked these candidates by also observing the optically thinner tracer $H^{13}CO^{+}$ 1–0. In all cases except for BGPS 2432, the $H^{13}CO^{+}$ peak velocity agreed with the NH₃ velocity within 0.2 km s⁻¹. Even in the case of BGPS 2432, where the velocity difference between $H^{13}CO^{+}$ and NH₃ was +0.57 km s⁻¹, both lines still peak within the HCO⁺ absorption dip. Thus, $H^{13}CO^{+}$ observations confirm that an optically thinner line peaks in the absorption dip for all six candidates. This result also indicates that the NH₃ (1, 1) and (2, 2) transitions are good tracers of the systemic velocity of the clumps, partly due to their multiple hyperfine lines with different optical depths. In the subsequent analysis, we consider the six sources (BGPS 2432, BGPS 3300, BGPS 3302, BGPS 3604, BGPS 4029, and BGPS 5021) as inflow candidates.

All of the six inflow candidates have an HCO^+ absorption dip that is slightly red of the NH_3 or $H^{13}CO^+$ peak velocities. This effect has been observed in other inflow surveys (He et al. 2016; Jin et al. 2016). As described in Jin et al. (2016), global collapse (i.e., in competitive accretion models) could potentially create a redshifted absorption dip. This can be tested with higher-resolution observations; at the single-dish resolution of observations in this paper, these sources remain only candidates for global inflow.

A visual analysis of the spectra is not a robust quantitative measure of the asymmetry in the line profile; therefore, we use δv to measure the velocity shift between HCO⁺ and NH₃. δv

was first defined by Mardones et al. (1997):

$$\delta v = \frac{v_{\text{HCO}^+} - v_{\text{NH}_3}}{\Delta v_{\text{NH}_3}},\tag{2}$$

where ν_{HCO^+} is the peak HCO⁺ velocity, ν_{NH_3} is the peak NH₃ velocity, and $\Delta\nu_{NH_3}$ is the FWHM line width of the NH₃ lines. Ammonia parameters were taken from Svoboda et al. (2016). With this measure, if $\delta\nu$ is negative, it has blue asymmetry. If it is positive, it has a red asymmetry.

Figure 7 shows the histogram of δv values for the observed SCC sample (also see Table 1). Most of the sources are clustered within the range of $-2 \le \delta v \le 2$. One notable exception is the source BGPS 3125, with a $\delta v < -4$. Visual inspection of the source indicates that the HCO^{+} 1–0 is a rare example of a triplepeaked spectrum with the NH₃ well aligned with a weaker peak in HCO⁺. Therefore, BGPS 3125 is not a good infall candidate, and its large negative δv should be ignored. All of the six best infall candidates have $\delta v < -0.48$. Of the remaining sources with $\delta v < -0.5$, eight of the sources are single peaked in HCO⁺ with no self-absorption dip, two sources are double peaked but the peaks are nearby equal in height (BGPS 2533 and BGPS 3151), one source is double peaked but a poor inflow candidate owing to NH₃ not peaking within the self-absorption dip (BGPS 2984), and three sources have more than two peaks in HCO⁺. See Figures 4 and 5 for spectra of all observed clumps.

There is a very slight bias of blue asymmetry over red asymmetry in our observed δv distribution. We use the definition of blue excess given in Mardones et al. (1997):

$$E = \frac{N_{\text{blue}} - N_{\text{red}}}{N_{\text{total}}},\tag{3}$$

where $N_{\rm blue}$ is the number of blue asymmetric profiles, $N_{\rm red}$ is red asymmetric, and $N_{\rm total}$ is the total number of clumps in our sample. Using the limit that a δv of less than -0.25 is a significant blue asymmetry and one of greater than 0.25 is a significant red asymmetry (since the ± 0.25 threshold is approximately 5 times our median error in δv), we then have $N_{\rm blue}=35$ clumps and $N_{\rm red}=32$ clumps. This leaves another 32 clumps that had a δv value between -0.25 and 0.25 (the total number of clumps with a valid δv value is 99 clumps). Using these values, we come to a blue excess of E=0.03.

Compared to other surveys that calculated the blue excess also using HCO⁺, our value for blue excess is on the low end. Fuller et al. (2005), Purcell et al. (2006), Wu et al. (2007), He et al. (2015), and Rygl et al. (2013) have each completed a survey of various stages of star formation while using the chemical tracer HCO⁺. Four out of the five of the surveys found excess values near E = 0.2, while one found a value near ours at E = 0.02. He et al. (2015) and He et al. (2016) used the MALT90 survey data (Jackson et al. 2013) to calculate their blue excess, and their prestellar objects were most similar to our sample of SCCs; clumps with no mid-infrared sources were identified by a flux cut in the ATLASGAL survey. We found a larger fraction of objects with red excess as compared to their results. We should note that there is significant difference in the definition of an inflow candidate given by He et al. (2016) and our paper; namely, we require the line profile to have a blue asymmetry with a self-absorption profile, while the He et al. (2016) paper only required that the source have $\delta v < -0.25$ in at least one optically thick tracer and no red skewed profiles in any optically thick tracer. We find

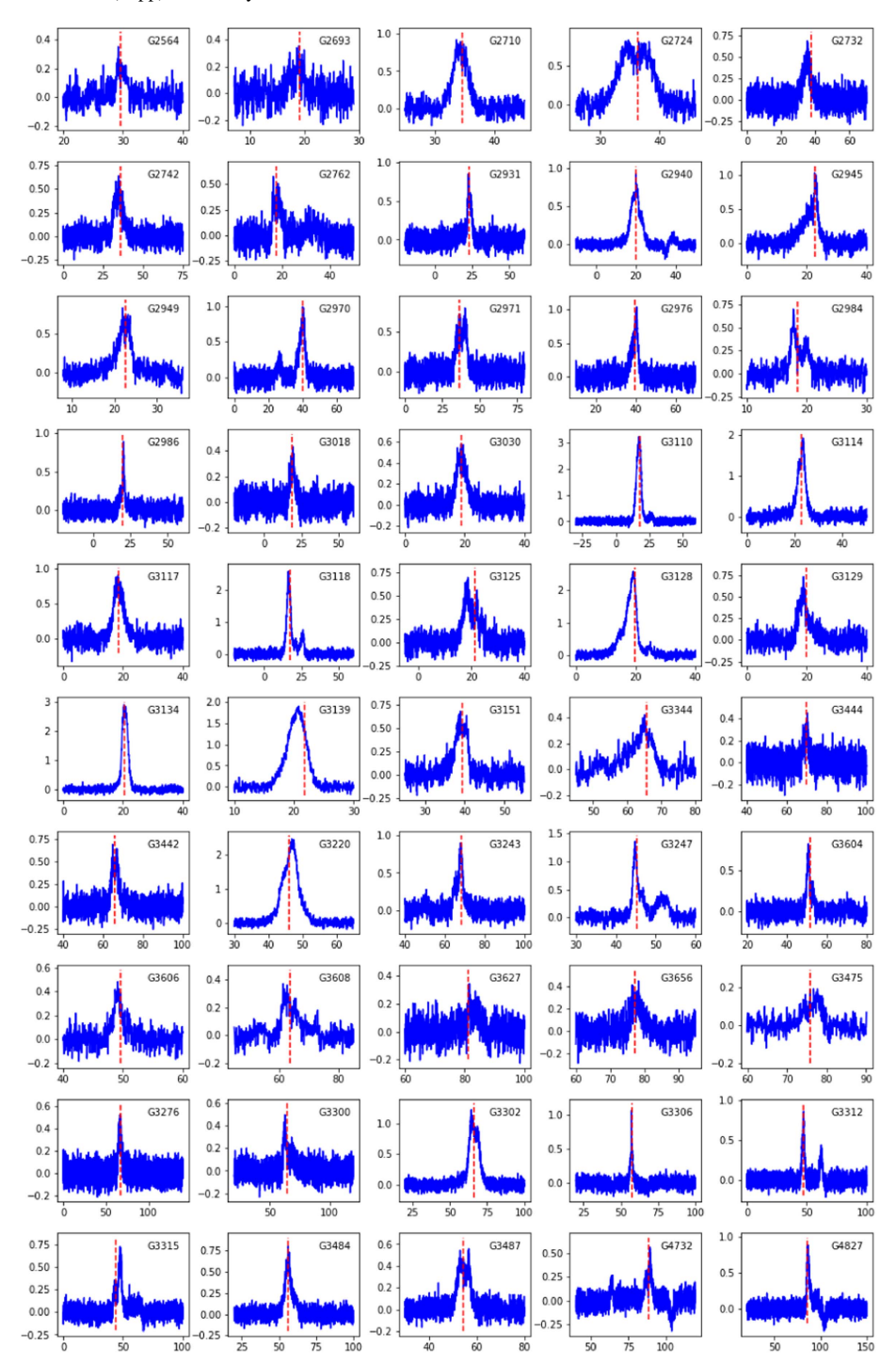


Figure 4. Line profiles of the first half of the 99 clumps that have detections in HCO^+ . The y-axis is in km s⁻¹, and the x-axis is in kelvin. The red dashed line shows the observed ammonia peak.

several sources with $\delta \nu < -0.5$ but that are single peaked in HCO⁺ 1–0. With a single pointing survey and a large beam that encompasses the entire clump, we cannot confidently claim that these large negative $\delta \nu$ single-peaked HCO 1–0 sources are good inflow candidates; the observed velocity offset between HCO⁺ and NH₃ may be due to variations in the chemical or excitation structure of the clumps. In addition to this, our sample was selected blindly from SCCs that had previously been detected in NH₃ emission, while the MALT90 prestellar clumps were selected from a flux cut and therefore represent the brightest ATLASGAL clumps in that category.

The only study with a blue excess similar to ours is that of Purcell et al. (2006), which observed methanol masers associated with massive YSOs. It is likely that their E=0.02 is contaminated by strong outflow motions associated with massive protostars that can create a red asymmetric line profile. Our survey is unique in that we are observing the earliest stage of star formation where there should not be strong contamination due to outflows from intermediate- or high-mass stars. With our value of E=0.03 we see that the earliest stages of star formation do not strongly favor blue or red asymmetric HCO^+ 1-0 line profiles for BGPS starless clump candidates.

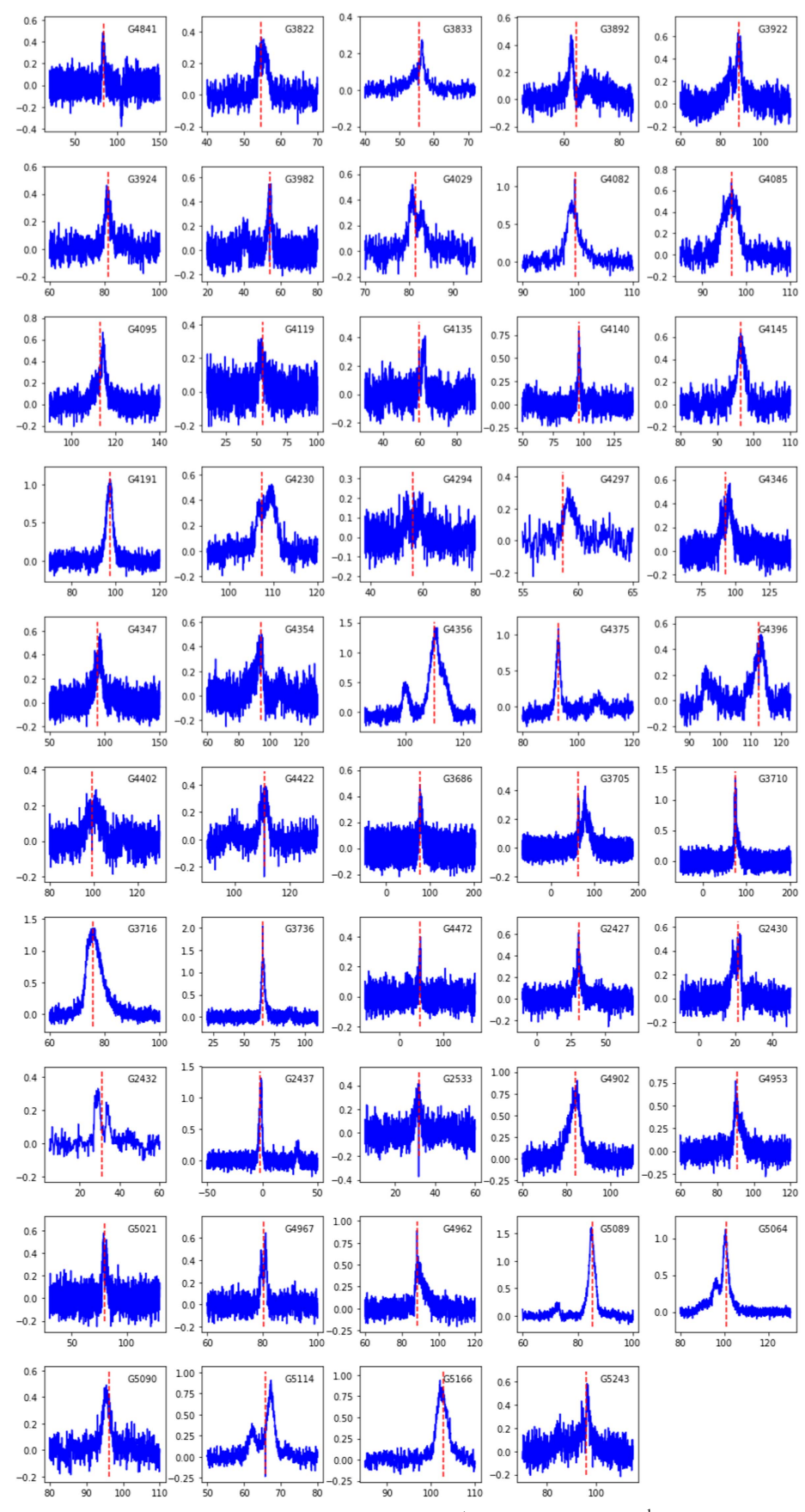


Figure 5. Line profiles of the second half of the 99 clumps that have detections in HCO $^+$. The y-axis is in km s $^{-1}$, and the x-axis is in kelvin. The red dashed line shows the observed ammonia peak.

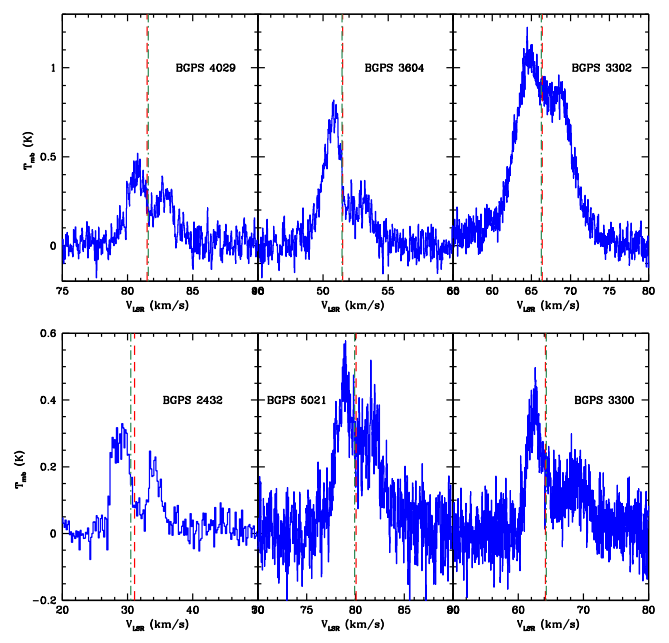


Figure 6. Line profiles of our best inflow candidates. Each profile has blue asymmetry with an NH_3 peak (shown as the red dashed line) and an $H^{13}CO^+$ peak (shown as a green dotted-dashed line) in the self-absorption dip. These were the only sources that met these two criteria and had reasonable inflow velocities as modeled in Section 4.

3.2. Comparison with Physical Properties of the Clumps

We compared δv to the virial parameter and clump mass as seen in Figure 5. There is no strong relationship between δv and the mass, meaning that given a certain clump's mass we cannot accurately predict that same clump's δv value. We might have expected there to be a slight relationship that suggested that more massive clumps were more likely to have a blue δv value, since the more massive clumps might be more likely to be gravitationally collapsing, but we observe no trend.

Another indicator of the potential for gravitational collapse is the virial parameter, $\alpha_{\rm vir}$. An $\alpha_{\rm vir} < \sim 2$ signifies that a clump is gravitationally bound and may undergo collapse. Many of our clumps are defined as gravitationally bound, but the δv value once again does not correlate with this parameter. It is important to note that in our calculation of $\alpha_{\rm vir}$ we only account for kinetic and potential energy and not for external pressure or magnetic field support. As discussed in Svoboda et al. (2016), a modest magnetic field of only a few hundred microgauss is needed to raise the typical SCC virial parameter above 2. A proper virial analysis also needs to consider the weight of the surrounding cloud on the clump and turbulent surface pressure (see Kirk et al. 2017).

We were unable to find any significant trend between δv and physical parameters of the clumps. This statement includes the six best inflow candidates, which are not strongly clustered in mass or virial parameter. Our lack of correlation is in contrast to the recent survey of 17 massive clumps that are 70 μ m dark by Traficante et al. (2018), which did find a correlation between HCO⁺ 1–0 line asymmetry (defined in a different method than used here) and the peak mass surface density of the clumps; however, the peak surface densities in our survey are generally lower (see Figure 3) than the 0.1 g cm⁻³ threshold for which they observe more asymmetric line profiles.

4. Analysis and Discussion

Only 6% of observed starless clump candidates show a signature of inflow in HCO^{+} 1–0. This result, taken without caveats, indicates either that large-scale inflow motions are a rare occurrence in our Galaxy or that a global initial inflow process during the starless phase is very quick and is therefore only observable in a few percent of clumps. Svoboda et al. (2016) estimated the starless phase lifetime of clumps and showed that the phase lifetime varied inversely with the mass of the clumps. If the low percentage of observable inflow signatures is attributable to a brief massive inflow phase, then the Svoboda et al. (2016) relationship indicates that this massive global inflow starless phase lasts \sim 60,000 yr for the median inflow candidate in our sample. However, we must consider the caveats, as there are many different factors that could result in nondetection of inflow. The detection of a blue asymmetric profile requires a specific set of conditions, namely, increasing excitation temperature along the line of sight, being optically thick along the line of sight, and a favorable line-ofsight velocity field. Simulations of global collapse show that there is a directional efficiency factor of up to $\sim 50\%$ for observing blue asymmetric line profiles with common dense gas tracers (Smith et al. 2012, 2013), meaning that our observed inflow detection rate of 6% could be 12% in reality. Furthermore, we are only sensitive to motions that are fast enough to produce a measurable blue asymmetry, meaning that a slow flow comparable to the FWHM line width observed in our large beam will not be detected. Radiative transfer simulations (Smith et al. 2013) also show that larger beam sizes suppress blue asymmetries. Thus, our observational result is likely a lower limit to the number of clumps with detectable inflow. In this section, we shall model and analyze the profiles of the best inflow candidates, calculate the mass inflow rate, and calculate the total change in mass of the clump in a freefall time.

We model our best inflow candidates using the analytic HILL5 model from De Vries & Myers (2005) with five parameters: τ_0 , the optical depth at the peak observed line temperature $T_{\rm pk}$; $v_{\rm in}$, the inflow velocity; $v_{\rm LSR}$; and σ , the line width. The HILL5 model solves the equation of radiative transfer with the assumption that the excitation temperature is a linear function of optical depth (a "HILL" model). De Vries & Myers (2005) found that the five-parameter version of the HILL model most consistently and accurately recovered the inflow velocity when fit to synthetic spectra created from radiative transfer models compared to other parameterizations of the HILL model and the simpler "two-layer" model of Myers et al. (1996). We apply Bayesian parameter estimation to fit the HILL5 model independently to each HCO^{+} 1–0 spectrum. We use the affine-invariant Markov chain Monte Carlo (MCMC) ensemble sampler emcee (Foreman-Mackey et al. 2013) to maximize its log-likelihood function

$$\ln p(T|\boldsymbol{\theta}) = -\frac{1}{2} \sum_{n} \left[\frac{(T_{n} - f_{h5}(\boldsymbol{\theta}))^{2}}{\sigma_{T}^{2}} \right]$$
 (4)

over each channel n in the spectrum with observed main-beam temperature $T_{\rm n}$, uniform baseline rms σ_T , and HILL5 model value (Equation (4)) for parameter set θ . Uniform priors were chosen with ranges of $\tau_0 = 0$ –10, $\Delta v_{\rm LSR} = \pm 3\,{\rm km\,s^{-1}}$, $v_{\rm in} = 0$ –1 km s⁻¹, $\sigma = 0$ –10 km s⁻¹, and $T_{\rm pk} = 0$ –100 K. This range was chosen to accommodate the range of physical values while

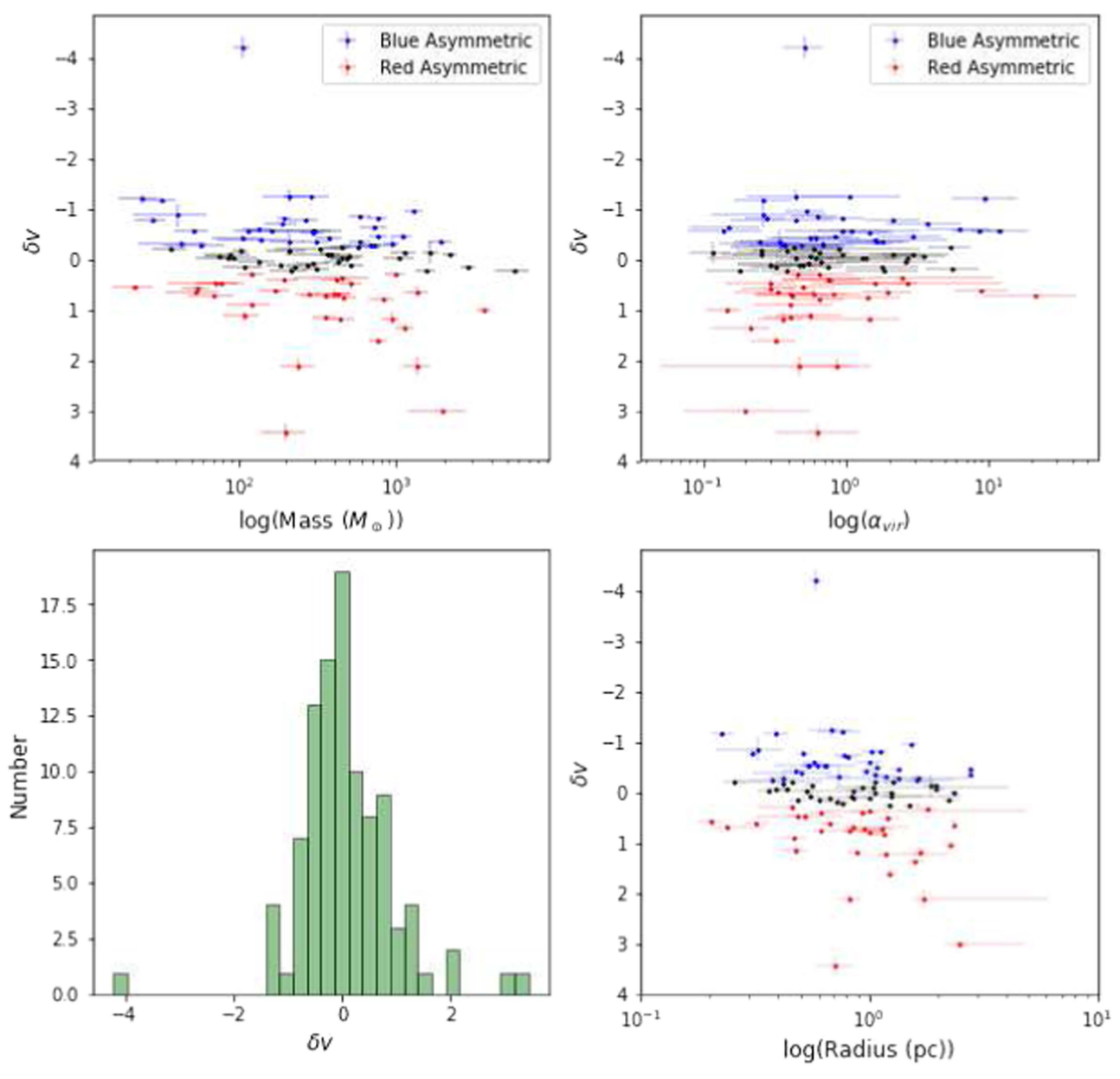


Figure 7. We compare δv to mass (top left panel), virial parameter (top right panel), and clump radius (bottom right panel). The histogram of δv values is shown in the bottom left panel. There is no obvious correlation present in the three δv comparison graphs. The Spearman rank coefficient of these three plots is 0.19 for mass, -0.12 for virial parameter, and 0.18 for radius. The red points are clumps with a red asymmetry $\delta v > +0.25$, and the blue points are clumps with a blue asymmetry $\delta v < -0.25$, while black points fall in a middle range of δv .

preventing nonphysical solutions when the model spectra extend outside the data range. Initial guesses start with $\tau_0=1$, $\Delta \nu_{\rm LSR}=0\,{\rm km~s}^{-1}, \nu_{\rm in}=0\,{\rm km~s}^{-1}, \sigma=\sigma_{\rm NH_3}\,{\rm km~s}^{-1},$ and $T_{\rm pk}=2T_{\rm HCO^+}\,{\rm K}.$

We find good fits to all of the best inflow candidates (Figure 8), with inflow velocities that range from 0.25 to 0.84 km s⁻¹. The median inflow velocity is 0.72 km s⁻¹, and the median uncertainty from the MCMC analysis is 0.13 km s⁻¹. These motions, if attributed to inflow, are supersonic. Unsurprisingly, the HILL5 model is consistent with zero inflow velocity in these two cases. The inflow velocities are plotted versus mass of the clumps in the Figure 9. The inflow velocities do not correlate with the mass of the clumps; however, the inflow candidates with masses below the median $300 \, M_{\odot}$ of the sample all tend to have the largest inflow velocities.

The inflow velocities are plotted versus mass of the clumps in Figure 7. The inflow velocities do not correlate with the mass of the clumps; however, the inflow candidates with masses below the median $300\,M_\odot$ of the sample all tend to have the largest inflow velocities.

Using the inflow velocity estimated by our HILL5 modeling, we calculate the mass inflow rate taken from López-Sepulcre et al. (2010):

$$\dot{M} = 4\pi R^2 v_{in} \rho = \frac{3Mv_{in}}{R}
= 3068 \frac{M_{\odot}}{\text{Myr}} \left(\frac{M}{1000 M_{\odot}}\right) \left(\frac{v_{in}}{1 \text{ km s}^{-1}}\right) \left(\frac{1 pc}{R}\right).$$
 (5)

The highest inflow rate is BGPS 3302, with $1880 M_{\odot} \,\mathrm{Myr}^{-1}$, and the lowest inflow rate is BGPS 4029, with $520 M_{\odot} \,\mathrm{Myr}^{-1}$. We

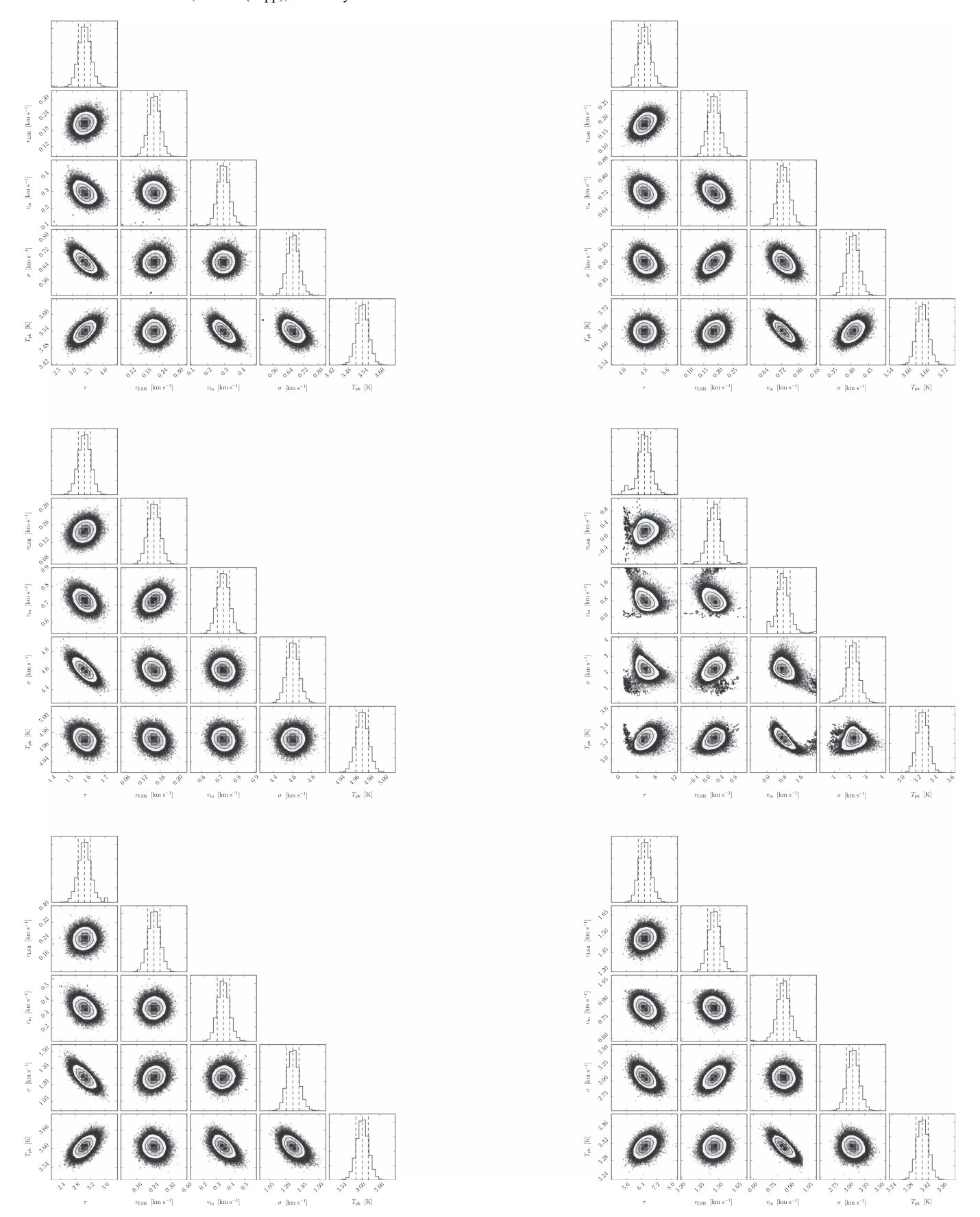


Figure 8. Triangle plots of the results of the five HILL5 modeling parameters (τ , v_{LSR} , v_{in} , σ , and T_{pk}) for the best infall candidates. Shown starting from the upper left are 4029, 3604, 3302, 2432, 5021, and 3300 ending at the lower right.

Table 2
Inflow Candidates

Source	(km s^{-1})	$(\operatorname{km}^{\sigma_{vin}}_{s^{-1}})$	t _{ff} ^a (Myr)	$(M_{\odot} \text{ Myr}^{-1})$	$\Delta M \ (M_{\odot})$	$\Delta M/M$
BGPS 2432	0.718	0.196	0.661	823	544	2.9
BGPS 3300	0.841	0.165	0.871	607	529	3.2
BGPS 3302	0.723	0.034	0.751	1876	1408	1.4
BGPS 3604	0.728	0.119	0.704	748	526	2.8
BGPS 4029	0.296	0.130	0.593	521	309	0.7
BGPS 5021	0.347	0.082	0.694	567	393	1.0

Note.

^a The median of the freefall probability density function calculated in Svoboda et al. (2016).

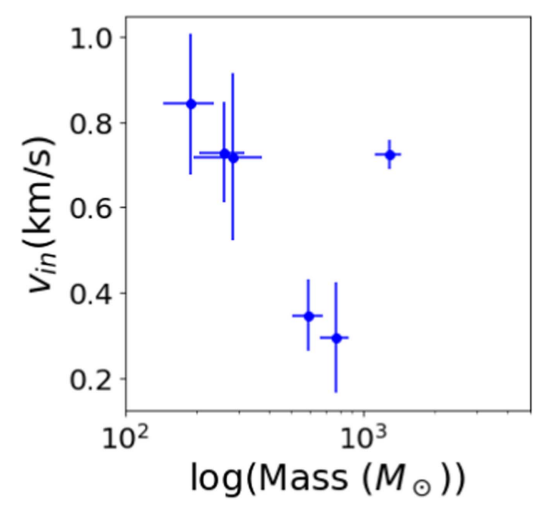


Figure 9. Here we show the relationship between infall velocity as modeled by HILL5 and clump mass. We do not find any significant correlation here. The Spearman rank correlation coefficient is -0.66. We are working with a low number of objects, and our δv analysis showed that there is no correlation between radius (a factor in $v_{\rm in}$) and inflow likelihood as represented by δv . (See Figure 7).

are assuming complete symmetrical collapse of the clump with all of the mass of the clump participating in the inflow motions. The calculated mass inflow rate will be an overestimate if only a fraction of the mass of the clump is associated with inflow motions within the 12 m telescope beam. On the other hand, we only measure velocities along the line of sight, and this geometry likely underestimates the inflow velocity and subsequent mass accretion rate. It is not clear which factor would dominate, and therefore our mass accretion rates are highly uncertain.

Large-scale inflow has been observed in both high-mass and low-mass star-forming regions. Peretto et al. (2013) studied star-forming regions centered at a massive inflowing filament, similar to the type of object we are searching for. They found a mass inflow rate of $2500 \pm 1000\,M_\odot\,\mathrm{Myr}^{-1}$, which overlaps with the upper range of \dot{M} seen in our sample; however, this clump is known to already be forming massive stars and is not starless. Liu et al. (2017) observed large-scale inflows near $1000\,M_\odot\,\mathrm{Myr}^{-1}$ from maps of HCO+ 1–0 toward three protostellar BGPS clumps that were also observed in the MALT90 survey. Barnes et al. (2010) observed a dense molecular core undergoing gravitational collapse and also used Hill5 modeling and HCO+ observations. They found a mass inflow rate of $3400 \pm 1700\,M_\odot\,\mathrm{Myr}^{-1}$, which is a higher rate

than most of our candidates but does overlap with our highest inflow rates. Kirk et al. (2013) observed a filament inflowing into a central region in the intermediate-mass Serpens starforming cloud and found that along the filament $\dot{M} =$ $30~M_{\odot}\,\mathrm{Myr}^{-1}$ and radially the rate was $130~M_{\odot}\,\mathrm{Myr}^{-1}$. These values are smaller than the range in which we observe; however, the object they were observing was lower in mass than our inflow candidates ($\sim 20 \, M_{\odot}$ in the filament). It is doubtful that we could detect such low inflow rates toward BGPS SCCs given the modest line widths and our requirement that we observe a clear self-absorption dip in the HCO^{+} 1–0 line profile. Setting a lower limit of $v_{\rm in} = 0.2 \, {\rm km \, s^{-1}}$ to produce a self-absorption dip for the typical BGPS SCC line width, then for a 0.5 pc, $100 M_{\odot}$ clump we have a limiting detectable mass inflow rate of $\sim 120 \, M_{\odot} \, \mathrm{Myr}^{-1}$. Thus, it is entirely possible that we have missed the types of inflow deteced in the Serpens star-forming region and are only detecting massive, large-scale flows.

The candidate inflow clumps in our survey appear to be in an earlier phase than the examples where large-scale flows are observed, which are described above. The only published inflow survey of comparable objects with calculated mass inflow rates is the study of He et al. (2016), which analyzed spectra toward prestellar clumps observed in the ATLASGAL and MALT90 surveys. The objects are classified as prestellar based on the lack of mid-infrared or far-infrared compact source emission. He et al. (2016) find a median mass inflow rate of $2600 \, M_{\odot} \, \mathrm{Myr}^{-1}$, which is higher than our mass inflow estimates and comparable to the mass inflow rate observed by Peretto et al. (2013) toward a massive star-forming hub-filament complex. The He et al. (2016) inflow sample is generally more massive (500 M_{\odot}) and has higher peak mass surface densities (0.14 g cm⁻³) by a factor of 3-4 than our sample. As noted in Section 3.1, our constraints to qualify a source as an inflow candidate are more stringent than in He et al. (2016).

For our six best inflow candidates, we calculate the change in mass of the clump assuming a constant mass accretion rate over the average clump freefall time ($\Delta M = \dot{M}t_{\rm ff}$). Using the median freefall time for each clump calculated in Svoboda et al. (2016), we find that BGPS 4029 has the lowest ΔM of 310 M_{\odot} and BGPS 2432 has the highest value of 1410 M_{\odot} . If we divide the total change in mass during the freefall time by the mass of the clump, we find that most of the clumps would double in mass over a freefall time (See Table 2). It should be noted that the freefall time corresponds to the time for the clump to collapse at the average clump volume density and corresponds to a median value of 0.7 Myr for the inflow candidates. This timescale is longer than the median gas

depletion timescale of $M/\dot{M}=0.5$ Myr for the inflow candidates, which may indicate that the clumps are growing in mass from the surrounding medium. While most SCCs may have a phase lifetime longer than their clump-average freefall timescale (Svoboda et al. 2016), the inflow candidates may be rare examples of clumps that are in a phase where they are embedded within a supersonic flow and are growing in mass at a significant rate.

Our single-dish survey, while a good first step for identifying promising inflow candidates, cannot exclude the possibility that observed line profiles are due to unresolved motions between dense cores within the clump. Furthermore, our analysis of the mass inflow rates has made the very simple assumption that the total mass of the clump is associated with the inflow motions. These objects are clearly interesting targets for higher-resolution observations (i.e., with ALMA) that can directly address these caveats.

5. Conclusions

We observed 101 massive starless clump candidates from the BGPS survey using the optically thick, intermediate-density gas tracer HCO^+ J = 1-0. We found that only six clumps (6%) had line profiles that had a self-absorption dip at nearly the same velocity (slightly redshifted) as the peak of NH₃ (1,1) emission and had an HCO^+ 1–0 peak intensity blueward of its self-absorption dip (blue asymmetry). The complete sample of SCCs has a small blue excess of only E = 0.03, indicating that blue asymmetric line profiles are rare toward BGPS starless clump candidates in HCO^{+} 1–0. We found no correlation between δv and the physical parameters of the clumps, such as mass and virial parameter. Using HILL5 radiative transfer modeling of the best inflow candidates, we determine inflow velocities and mass inflow rates that range from 500 to $2000 \, M_{\odot} \, \mathrm{Myr}^{-1}$. At these accretion rates, the SCCs would double in mass over a freefall time. These clumps may be in a phase where they are embedded within a supersonic inflow and are growing in mass at a significant rate.

The 12 m ARO telescope has a beam size that is about the same size as or slightly larger than the clump radii we were observing. As a result, our six inflow candidates are only candidates for inflow motions. Higher spatial resolution mapping observations on telescopes such as the GBT and ALMA are necessary to confirm whether these objects are truly starless and whether they have global inflow motions.

We sincerely thank the staff and operators of the Arizona Radio Observatory. J.K.C., B.E.S., and Y.L.S. are supported in part by NSF grant AST-1410190. B.E.S. is also supported by the NSF Graduate Research Fellowship under grant no. DGE-

114395. J.K.C. thanks the Arizona NASA Space Grant Consortium for internship support.

Facility: ARO:12m.

Software: ds9, GILDAS CLASS.

References

```
Barnes, P. J., Yonekura, Y., Ryder, S. D., et al. 2010, MNRAS, 402, 73
Choi, M., Evans, N. J., II, Gregersen, E. M., & Wang, Y. 1995, ApJ, 448, 742
De Vries, C. H., & Myers, P. C. 2005, ApJ, 620, 800
Eden, D. J., Moore, T. J. T., Plume, R., et al. 2017, MNRAS, 469, 2163
Elia, D., Molinari, S., Schisano, E., et al. 2017, MNRAS, 471, 100
Ellsworth-Bowers, T. P., Rosolowsky, E., Glenn, J., et al. 2015, ApJ, 799, 29
Evans, N., II 2003, SFChem 2002: in Chemistry as a Diagnostic of Star
  Formation, ed. C. L. Curry & M. Fich (Ottawa: NRC Press), 157
Evans, N. J., II, Lee, J.-E., Rawlings, J. M. C., & Choi, M. 2005, ApJ, 626, 919
Feng, S., Beuther, H., Zhang, Q., et al. 2016, A&A, 592, A21
Foreman-Mackey, D., Hogg, D. W., Lang, D., & Goodman, J. 2013, PASP,
Fuller, G. A., Williams, S. J., & Sridharan, T. K. 2005, A&A, 442, 949
Ginsburg, A., Glenn, J., Rosolowsky, E., et al. 2013, ApJS, 208, 14
He, Y.-X., Zhou, J.-J., Esimbek, J., et al. 2015, MNRAS, 450, 1926
He, Y.-X., Zhou, J.-J., Esimbek, J., et al. 2016, MNRAS, 461, 2288
Hoq, S., Jackson, J. M., Foster, J. B., et al. 2013, ApJ, 777, 157
Jackson, J. M., Rathborne, J. M., Foster, J. B., et al. 2013, PASA, 30, e057
Jin, M., Lee, J.-E., Kim, K.-T., & Evans, N. J., II 2016, ApJS, 225, 21
Kirk, H., Friesen, R. K., Pineda, J. E., et al. 2017, ApJ, 846, 144
Kirk, H., Myers, P. C., Bourke, T. L., et al. 2013, ApJ, 766, 115
Liu, X.-L., Xu, J.-L., Ning, C.-C., Zhang, C.-P., & Liu, X.-T. 2017,
  arXiv:1709.08391
López-Sepulcre, A., Cesaroni, R., & Walmsley, C. M. 2010, A&A, 517, A66
Mangum, J. G. 1993, PASP, 105, 117
Mangum, J. G., & Shirley, Y. L. 2015, PASP, 127, 266
Mardones, D., Myers, P. C., Tafalla, M., et al. 1997, ApJ, 489, 719
Matzner, C. D. 2017, arXiv:1712.01457
McKee, C. F., & Ostriker, E. C. 2007, ARA&A, 45, 565
Motte, F., Bontemps, S., & Louvet, F. 2017, arXiv:1706.00118
Myers, P. C., Bachiller, R., Caselli, P., et al. 1995, ApJL, 449, L65
Myers, P. C., Mardones, D., Tafalla, M., Williams, J. P., & Wilner, D. J. 1996,
    pJL, 465, L133
Narayanan, G., Walker, C. K., & Buckley, H. D. 1998, ApJ, 496, 292
Palmeirim, P., André, P., Kirk, J., et al. 2013, A&A, 550, A38
Peretto, N., Fuller, G. A., Duarte-Cabral, A., et al. 2013, A&A, 555, A112
Purcell, C. R., Balasubramanyam, R., Burton, M. G., et al. 2006, MNRAS,
Rygl, K. L. J., Wyrowski, F., Schuller, F., & Menten, K. M. 2013, A&A,
  549, A5
Seo, Y. M., Hong, S. S., Lee, S. H., et al. 2011, ApJ, 736, 153
Shirley, Y. L. 2015, PASP, 127, 299
Shirley, Y. L., Ellsworth-Bowers, T. P., Svoboda, B., et al. 2013, ApJS, 209, 2
Smith, R. J., Hosokawa, T., Omukai, K., Glover, S. C. O., & Klessen, R. S.
  2012, MNRAS, 424, 457
Smith, R. J., Shetty, R., Beuther, H., Klessen, R. S., & Bonnell, I. A. 2013,
Svoboda, B. E., Shirley, Y. L., Battersby, C., et al. 2016, ApJ, 822, 59
Tafalla, M., Mardones, D., Myers, P. C., et al. 1998, ApJ, 504, 900
Traficante, A., Fuller, G. A., Smith, R. J., et al. 2018, MNRAS, 473, 4975
Urquhart, J. S., Csengeri, T., Wyrowski, F., et al. 2014, A&A, 568, A41
Wu, Y., Henkel, C., Xue, R., Guan, X., & Miller, M. 2007, ApJL, 669, L37
Zhang, T., Wu, Y., Liu, T., & Meng, F. 2016, ApJS, 224, 43
```